Supplementary Materials for

Gravity field of the Orientale basin from the Gravity Recovery and Interior Laboratory Mission

Maria T. Zuber,* David E. Smith, Gregory A. Neumann, Sander Goossens,
Jeffrey C. Andrews-Hanna, James W. Head, Walter S. Kiefer, Sami W. Asmar,
Alexander S. Konopliv, Frank G. Lemoine, Isamu Matsuyama, H. Jay Melosh,
Patrick J. McGovern, Francis Nimmo, Roger J. Phillips, Sean C. Solomon,
G. Jeffrey Taylor, Michael M. Watkins, Mark A. Wieczorek,
James G. Williams, Johanna C. Jansen, Brandon C. Johnson,
James T. Keane, Erwan Mazarico, Katarina Miljković,
Ryan S. Park, Jason M. Soderblom, Dah-Ning Yuan

*Corresponding author. Email: zuber@mit.edu

This PDF file includes:

Materials and Methods
Supplementary Text
Figs. S1 to S8
References

GRAIL's Mapping Mission

The GRAIL twin spacecraft, Ebb and Flow, orbited in tandem in polar orbit above the Moon and mapped the lunar gravity field at unprecedented resolution and accuracy. After insertion into lunar orbit on December 31, 2011 (Ebb), and January 1, 2012 (Flow), the spacecraft collectively executed a succession of 19 maneuvers to achieve the science orbit and mapping configuration. GRAIL's Primary Mission (PM) (*41*), which commenced on March 1, 2012, consisted of 89 days of mapping over three 27.3-d global mapping cycles at an orbit inclination of 89.9° and a mean altitude of 55 km. In practice the orbits deviated from circular due to perturbations from the lunar gravity field. When the solar orientation became unfavorable for satellite-to-satellite ranging on May 30, 2012, the spacecraft discontinued mapping and the orbits were raised to a mean altitude of 84 km.

During GRAIL's Extended Mission (XM), which commenced on August 30, 2012, the dual spacecraft orbited above the lunar surface at a mean altitude of 23.5 km (*8*), less than half the mean mapping altitude in the PM. The low-altitude XM orbit was maintained by executing 2–3 weekly maneuvers (*42*).

Subsequent to a lunar eclipse on November 28, 2012, the mean altitude of the orbiters was decreased by another factor of two to 11.5 km, for additional mapping (Fig. S1). The principal objective of this Endgame mission phase was to perform mapping of the Orientale basin at the highest possible resolution. The low altitude of the spacecraft and variation of topography, coupled with the variability of the lunar gravity field, dictated that the orbital altitude coverage over the basin was non-uniform (Fig. S2), with the lowest altitudes achieved in the eastern part of the basin and in particular over the basin rings, which were mapped from 2-km altitude. GRAIL's science mapping was completed on December 14, after which a series of engineering experiments was executed prior to planned impact of the spacecraft onto the lunar surface on December 17, 2012.

GRAIL Global Gravity Solutions

The global gravity field of a planetary body is typically represented in spherical harmonics, which are solutions to Laplace's equation for the gravitational potential on a sphere. In practice, the resolution of gravity measured from a spacecraft will depend on both coverage and spacecraft attitude, and so it is common for unmodeled signal to be present even for high-degree and -order gravity field solutions. Published gravity models that incorporate global data from the GRAIL PM are to degree and order 660 (spatial block size = 8.3 km) (*43, 44*), and published models that incorporate observations from both the PM and XM are to degree and order 900 (spatial block size = 6.0 km) (*11, 45*). The analysis in this paper uses a degree- and order-1200 (spatial block size = 4.5 km) field, produced in the manner of our previously published models (*20*). Due to the varying spacecraft altitude which was a combined consequence of the lunar topography and perturbations to spacecraft orbits by the uneven subsurface mass distribution, the full resolution of this global model is achieved only in the areas of lowest-altitude mapping. Orientale contains the lowest-altitude coverage of the GRAIL mission, due to a decision to produce a map at the highest-possible-resolution map of this important structure. The Orientale map from the degree- and order-1200 field was produced at the Jet Propulsion Laboratory.

Local Modeling Using Short-arc Analysis

As an alternative approach to achieving the highest-resolution map permitted by the data, we developed a local model of the gravitational signature of Orientale that utilized the residual signal remaining from a gravity model to degree and order 900. We analyzed GRAIL's complete XM and endgame Ka-band range rate (KBRR) tracking data from 240° to 300° E longitude and -55° to 5° latitude. Data were analyzed in arcs of approximately 18-min duration. The short-arc analysis method (*10*) utilizes a spherical harmonic representation of the 12-epoch state parameters that quantitatively characterize the baseline between the satellites. First used to determine temporal gravity solutions (*46, 47*) using data from the Gravity Recovery and Climate Experiment (GRACE) mission (*48*), the method as applied to the Moon has been demonstrated with GRAIL observations over the lunar south pole (*49*).

The gravity field may be expressed with the Stokes formulation as a gravitational potential W:

$$W = U + T \tag{S1}$$

where U is the normal potential of a reference field on a body with radius R, and

$$T(P) = \frac{R}{4\pi} \int_\sigma S(P,Q)\Delta g(Q)d\sigma \tag{S2}$$

is the disturbing potential, where the integration is taken over the surface σ, $S(P,Q)$ is the Stokes-Pizetti kernel (*50*) with P the point at which the potential is computed and Q a point on σ, and the gravity anomalies (Δg) may, with a spherical approximation, be written

$$\Delta g = -\frac{\partial T}{\partial r} - 2\frac{T}{r} \tag{S3}$$

where r is the radial distance in spherical coordinates. If T is expressed in spherical harmonics, then the anomalies and spherical harmonics are equivalent and anomalies can be expressed in spherical harmonics by multiplying by a factor *(l -1)*, where *l* is the spherical harmonic degree. The partial derivatives of the KBRR data with respect to the anomalies can be obtained from the acceleration on the satellite by differentiating a version of equation (2) in which the integral has been replaced by a summation over the separate anomalies.

Given a GRAIL gravity model to degree and order 900 (*11*) as an *a priori* model, parameters that included the baseline vector pitch, baseline rate of change of vector magnitude, and baseline rate of change of vector pitch were adjusted using the Goddard Space Flight Center GEODYN II Orbit Determination and Geodetic Parameter Estimation Program (*51*). After adjusting these baseline parameters and converging the short arcs, GEODYN was again used to calculate partial derivatives of the KBRR data points with respect to the adjusted baseline parameters and selected gravitational field parameters. Local anomaly values (Δg_{adj}) were estimated with respect to the global model ($\Delta g_{GRGM900A}$)at the center coordinates of grid points. For our final model we applied a grid with mixed resolution, to account for the varying altitude above topography. For the area between 240° and 275° E longitude we used a resolution of 0.1667×0.1667 deg^2, whereas for the area between 275° and 300° E longitude, which included the lowest-altitude passes, we used a resolution of 0.1×0.1 deg^2. The maximum spatial resolution is thus 3 to 5 km.

We applied a neighbor-smoothing constraint (*52, 53*) to the full solution

$$\Delta g_{full} = \Delta g_{adj} + \Delta g_{GRGM900A}, \qquad\qquad\qquad\text{(S4)}$$

which, in addition to allowing the mapping of gravity anomalies to be extended to the highest resolution, had the benefit of mitigating high-degree striping evident in the spherical harmonic solution.

A comparison of residuals from the global spherical harmonic model with those from the local model is shown in Fig. S3 and illustrates the considerable improvement of the latter model. The average root mean square (RMS) residual of the KBRR fits over the Orientale region improves from 0.987 μm s^{-1} for the global model to 0.225 μm s^{-1} for the local model (77% improvement in residuals). The median of the fits improves from 0.629 μm s^{-1} to 0.160 μm s^{-1} (75% improvement in residuals).

Local and Global Map Comparison

The local model and degree-1200 global model are independent representations of the gravitational signature of Orientale produced from the same GRAIL tracking data set. The models are of comparable resolution and, as shown in Fig. S4, they show strikingly similar small-scale structure, which provides high confidence in the short-wavelength character of the map.

Bouguer Anomaly Field and Crustal Structure

In order to isolate subsurface density variations, we subtracted the gravitational attraction of surface topography from a spherical harmonic model to degree and order 1080 to yield a map of Bouguer gravity anomalies. The calculation is for a crustal density of 2550 kg m^{-3} (*20*). In the Bouguer anomaly plot in Fig. 1C we subtracted spherical harmonic degrees < 6 in order to highlight short-wavelength structure.

Crustal thickness was determined in a manner analogous to an earlier study using GRAIL gravity and LOLA topography by our group (*20*). In this work we exploit the considerable improvement of the XM data, with more than double the resolution of the data in the earlier study. Downward continuation of the Bouguer anomaly to a crust-mantle interface with an average radius of 1703.15 km yields an average thickness of 34 km and satisfies global constraints. The relief on this density interface produces a gravitational signal that matches the Bouguer anomaly up to a spherical harmonic degree and order determined by a constraint on its amplitude needed to regularize the solution in Fig. 2A. The iterative solution is stabilized by a damped correction to the previous solution to ensure convergence. The highest resolution of crust-mantle interface deemed physically plausible corresponds to a minimum amplitude downward continuation filter with a value of 0.5 at degree 240, or a spatial blocksize of approximately 23 km, limited by the ~50 km average depth of the annulus of thickened crust surrounding the mantle plug, and by the spatial variations in density not incorporated into the crustal model. The noise level of the gravity solution itself is not a limiting factor. We explored models with resolutions higher by a factor of 2–3, for which amplitudes approached the limiting noise level in the data. Spatial averaging over azimuthal sectors, as in Figure 2B, preserves the radial resolution of mantle relief coherent with ring structures, while suppressing signals from the shallower density variations in the crust. The azimuthal sectors shown in Fig. 1D are chosen to avoid large east-west gradients in elevation and crustal thickness.

The range of slopes of the region of uplifted mantle that results from a crustal inversion depends approximately linearly on the density contrast assumed between the

crust and mantle. However, the range depends even more on the filter used to stabilize the inversion, with higher slopes generally resulting when higher spherical harmonic degrees are passed by the filter than in the earlier inversion (*20*). Features that are revealed at higher resolution are suggestive of and consistent with fault displacements in the accompanying hydrocode calculation (*16*), although faults are virtually indistinguishable from more continuous relief and thus not necessarily required by the data.

Fig. S5 show radial profiles of surface topography and crust–mantle boundary relief that highlights the azimuthal variability of surface and subsurface structure. Within the inner depression, azimuthal variations in thickness are ±1 km. Outside the Inner Rook ring, azimuthal variations in crustal thickness are ±5–10 km, due in large part to azimuthal variability in the topography.

Effect of a High-density Melt Sheet on the Crustal Structure Model

Our inversion for crustal structure included provision for a surficial central sheet with higher density than the surrounding crust. This sheet could represent solidified impact melt that formed from crustal material but initially with zero porosity, an impact melt sheet that contained both mantle and crustal components, or more mafic crustal material formed by differentiation of the central impact melt pool.

An end-member model with no melt sheet contribution, a crustal density of 2550 kg m^{-3}, and a mantle density of 3220 kg m^{-3} (*20*) is consistent with some impact models in which cool crustal material migrates to the basin during basin collapse and covers initially exposed molten mantle material (*16, 54*). However, because the pre-impact lunar crust is largely to entirely removed by the impact (*35*), the crust that is measured by GRAIL at the basin center may be dominated by the solidified impact melt sheet.

Impact breccias and impact melt rocks from the Apollo 14, 15, 16, and 17 landing sites provide samples of impact rocks from the Imbrium, Nectaris, and Serenitatis basin-forming impacts. The measured bulk densities of 18 such rocks range from 2440 to 2830 kg m^{-3} (*25*). These bulk densities depend primarily on the amount of clastic material with pre-existing porosity in the breccias and the amount of vesicularity within the impact melt. Because of the high level of shock heating expected at the basin center, we do not anticipate a large abundance of clasts in the central melt sheet. The Apollo samples have an average melt sheet bulk density of 2720 kg m^{-3} for clast-poor impact melt rocks. Vesicularity should decrease with increasing depth (pressure), so it is possible that a slightly higher average bulk density is appropriate for the melt sheet.

An important consideration is the effect of differences in composition between the Orientale melt sheet and the Apollo impact melt samples. The Apollo samples have a mean FeO concentration of 6.8 weight % (range 3.1 to 9.2 %) and a mean TiO$_2$ concentration of 0.95 % (range 0.2 to 1.5%), whereas remote sensing observations indicate that the Orientale melt sheet (Maunder Formation) has mean FeO and TiO$_2$ concentrations of 4.4% and 0.6%, respectively (*55*). The scaling between composition and grain density of Huang and Wieczorek (*56*) suggests that the Orientale melt sheet is about 2.4% less dense than the Apollo samples. If the Orientale melt sheet and the Apollo impact melt samples have the same average porosity, this percentage reduction in density can also be applied to the bulk densities, implying a bulk density of 2650 kg m^{-3} for Orientale's melt sheet.

Relative to the typical feldspathic highland crust, the higher melt sheet density reduces the average density difference between crust and mantle and thus requires a thicker crust in the basin center. For a melt sheet density of 2650 kg m^{-3}, the minimum crustal thickness in the basin center is 10 km; a denser melt sheet of 2720 kg m^{-3} consistent with Apollo samples yields a minimum crustal thickness of 11 km. These minimum crustal thickness values are 2 and 3 km greater than a model in which the melt sheet has the same density of surrounding feldspathic crust (2550 kg m^{-3}). If the crust beneath the basin floor consists of a mixture of feldspathic crust (that either was not excavated or that flowed into the basin center from the surroundings during collapse of the transient cavity) and the impact melt pool, gravity data alone cannot constrain either the relative proportions of these materials or the thickness of the crust beneath the basin floor.

Composition of Crust Excavated by the Orientale Impact

Modeling the structural evolution of the Orientale basin requires knowing the lithologies of the crust beneath the basin. In our modeling we have assumed that anorthositic rock dominates the entire crustal column. However, lunar sample and remote sensing (*57*) data suggest that in the Procellarum KREEP Terrain [PKT, where KREEP is an acronym for lunar rocks enriched in potassium (K), rare earth elements (REE), and phosphorus (P)], of the lunar nearside, the lower crust is composed of rocks richer in olivine and pyroxene than the upper, plagioclase-rich crust. It is conceivable that this mafic lower crust is present everywhere on the Moon. Sample evidence includes the common occurrence so-called Low-K Fra Mauro (LKFM) impact melt breccias found at the Apollo 14-17 sites. Those at Apollo 15 and 17 are particularly important as the massifs sampled at those landing sites are rings of the Imbrium and Serenitatis basins, respectively. Remote sensing data (*57*) show extensive deposits of what appear to have compositions like LKFM surrounding and within the PKT.

We tested whether mafic ejecta material is present in the Orientale basin and its ejecta using remote sensing data of the region and the expected compositional signature of LKFM. Korotev (*58*) compiled bulk compositional data for samples of LKFM impact melt breccias from the Apollo 14–17 landing sites. Although compositions vary from site to site, the chief compositional characteristics are well defined: compared with the typical feldspathic crust, LKFM is markedly enriched in FeO and incompatible trace elements (Th, U, rare earth elements). Mineral abundances also differ: LKFM is enriched in low-Ca pyroxene and depleted in plagioclase compared with the feldspathic highlands. Olivine is variable in abundance and might represent mantle materials incorporated into the LKFM impact melts (*58*). Bearing in mind that LKFM is a mixture of a KREEP component, anorthosite, and a small component of olivine-rich rock (*58*), we can use Korotev's (*58*) compositional compilation and modal analyses of lunar samples (*59*) as guides to establish a chemical and mineralogical fingerprint of LKFM and use remote sensing data to search the Orientale basin structure for that signature.

Remote sensing data exist for the concentrations of FeO, Th, and major minerals. For FeO concentrations we use maps of Clementine surface reflectance data (binned to 1 km spatial resolution) and an iron-reflectance algorithm (*60*). For Th we use the Lunar Prospector Gamma-Ray Spectrometer (GRS) dataset (*61*) gridded at 0.5°, about 15 km spatial resolution. We use mineral data (*62*), which are derived from radiative-transfer-

based mineral maps (*63*), validated and improved by comparison with Lunar Prospector GRS elemental concentrations gridded to 2° bins. The minerals of interest for detecting mafic impact melt are plagioclase, low-Ca pyroxene, and olivine. The LKFM component contains, as estimated from data compilations (*58*)-(*59*), 7–11 wt% FeO, 5-10 ppm Th, 45–50 wt% plagioclase, 25–30 wt% low-Ca pyroxene, and 5–10 wt% olivine. These abundances are similar to the bulk composition of the impact melt sheet hypothesized to be present within the Orientale basin (*64*). We examined this set of remote chemical and mineralogical data to see if the hypothesized mafic, Th-rich crustal component is present in the Orientale region.

Results are shown in Fig. S6. Fig. S6A shows the topography of Orientale and its surroundings. The Inner Rook ring is outlined for reference and appears on all images in Fig. S6. The mare basalt fill in the middle of Orientale is clearly identifiable by its high FeO concentration (Fig. S6B). The region with lower FeO (~4 wt%) between the maria and the Inner Rook ring composes the Maunder Formation, thought to be impact melt (e.g., (*1, 5, 65*). A careful study of the composition of the basin interior (*55*) indicates that the Maunder Formation has an average FeO concentration of 4.4 ± 2.0 wt%. The Maunder Formation is low (~1.3 ppm) in Th (Fig. S6C), as are all basin deposits, except for the mare basalts. Thus, both FeO and Th concentrations in the exposed Orientale impact melt sheet (the Maunder Formation) are substantially lower than the ranges observed in LKFM rocks or in regions associated with the PKT. We suggest that the low FeO and Th concentrations rule out a substantial contribution of mafic lower crustal materials to Orientale surface deposits.

Taking a broad view of the composition of Orientale deposits, the impression is that it is composed of plagioclase-rich rock. All areas (except for the maria) contain at least 70 wt% plagioclase (Fig. S6-D), with many areas containing more than 85%. This result is consistent with the abundance of nearly pure anorthosite in numerous small areas (*66, 67*). Olivine and orthopyroxene abundances are generally less than 10 wt% and quite variable. Thus, the Orientale basin deposits all appear to be typical lunar feldspathic highlands, with no strong evidence for ejected lower crustal materials. We conclude that the assumption that the crust has the density of porous anorthite (2550 kg m^{-3}) (*20*), is appropriate for mapping the crustal structure outside of the Inner Rook ring. Within the Inner Depression, where the melt sheet is expected to be thickest, the melt sheet is largely covered by a thin veneer of mare basalt, and thus remote sensing does not constrain its composition. We therefore used Apollo sample data to estimate the density of the central melt sheet, as described above.

Excavated Volume

In determining the volume of material excavated by the Orientale impact we assumed a mean global crustal thickness of 34 km (*20*), a crustal density of 2550 kg m^{-3} (which for a 2900 kg m^{-3} grain density yields 12% porosity), and a mantle density of 3220 kg m^{-3}; these figures collectively satisfy the observations and a 30-km crustal thickness constraint at the sites of the Apollo 12 and 14 seismic stations (*68*).

In this model the median thickness is 42.7 km in the region surrounding Orientale (Fig. 1D, Fig. 2), and the base of the mantle plug extends to a depth of 43.5 km below the 1738-km-radius topographic datum.

An alternative model with a mean global crustal thickness of 43 km that corresponds

to a thickness of 38 km in the area of the Apollo seismic network (*69*) results in thicker crust at Orientale and a lower mantle density, which would effectively increase the volume of the mantle plug by approximately 10%.

In our crustal structure model, the average ejecta thickness of ~600 m is consistent with a recent estimate based on fill of pre-Orientale craters outside the basin cavity combined with simulations of crater erosion (*23*). This ejecta volume represents a downward revision from a previously published estimate (*70*). It is also consistent with a recent study of lunar crater outcrops that shows that ejecta accounts for no more than 20% of crater rim relief, with structural uplift the major contributor to rim development; as a consequence ejecta volumes and excavation depths may be factors of 3-4 less than previous estimations (*71*).

Polar-coordinate Maps of Orientale

To highlight surface and subsurface deviations from axisymmetry of Orientale, we plot the topography and gravity field versus polar coordinates about the basin center. A re-projection of the datasets in Fig. 1 is used for Fig. S8. To generate these "unwrapped" maps, we linearly interpolated the topography and gravity datasets on a grid of azimuth (measured clockwise from north) and radial distance with respect to the center of Orientale. The basin center (-19.3°N, 266.0°E) was chosen so the central Bouguer anomaly at the center of Orientale becomes as close as possible to axisymmetric in this projection. Linear interpolation of the original topography and gravity datasets is necessary in order to smooth the data toward the center of the basin, where latitude and longitude points are relatively widely spaced in these Cartesian projections with polar coordinates. After this transformation, radial features are vertical, parallel lines. Axisymmetric features (e.g., the Cordillera and Inner and Outer Rook rings) are horizontal, parallel lines. Elliptical features and axisymmetric features that are misaligned with the center of Orientale plot as sinusoids.

As with any two-dimensional Cartesian plot of circular or spherical data, these polar maps can distort relative sizes, shapes, and angles. As we are interested in identifying radial features within Orientale, we used a modified Mercator projection:

$$y = \begin{bmatrix} \ln\left(tan\left(90° - \frac{\theta}{2}\right)\right) & for\ d > 100\ km \\ (-3.2976 \times 10^{-4})\theta + 4.5479 & for\ d < 100\ km \end{bmatrix} \quad (S5)$$

where θ is the angular distance from the center of Orientale (which is related to distance d from the center by $\theta = d / (30.334$ km/degree)). At radial distances beyond 100 km from the center of Orientale, this projection is conformal (angles are preserved around all locations, and the horizontal and vertical scales around all positions are equal). Thus, the shapes of small features are preserved (e.g., craters are round), although the linear scale changes with distance from the center of Orientale. Like the polar regions of standard Mercator maps, this projection becomes unusable near the basin center. Thus, within 100 km of the center we use a linear relationship between y and θ within 100 km, constructed such that y(θ) is smooth and continuous at 100 km. Although this relation prevents the singularity at θ=0° found in the Mercator projection, the portion of the map within 100 km of the basin center is not conformal.

Bouguer Gravity Gradients

The gravity gradient quantifies the curvature of the Bouguer gravity field, which can be useful for identifying otherwise hidden density structures in the lunar interior (*72, 73*). The Bouguer gravity gradient is determined from the Bouguer gravity gradient tensor, $\bar{\bar{\Gamma}}$, which is a nine-component, symmetric tensor with five independent components constructed by taking gradients of the Bouguer gravity field:

$$\bar{\bar{\Gamma}} \equiv \begin{bmatrix} \frac{\partial g_x}{\partial x} & \frac{\partial g_x}{\partial y} & \frac{\partial g_x}{\partial z} \\ \frac{\partial g_y}{\partial x} & \frac{\partial g_y}{\partial y} & \frac{\partial g_y}{\partial z} \\ \frac{\partial g_z}{\partial x} & \frac{\partial g_z}{\partial y} & \frac{\partial g_z}{\partial z} \end{bmatrix} \equiv \begin{bmatrix} \Gamma_{xx} & \Gamma_{xy} & \Gamma_{xz} \\ \Gamma_{yx} & \Gamma_{yy} & \Gamma_{yz} \\ \Gamma_{zx} & \Gamma_{zy} & \Gamma_{zz} \end{bmatrix}, \tag{S6}$$

where g_x, g_y, , and g_z are the components of the Bouguer gravity field in a local Cartesian reference fame. As we are primarily interested in the horizontal gravity gradients ($\Gamma_{xx}, \Gamma_{xy}, \Gamma_{yy}$), we evaluate the eigenvalues of the horizontal gradient tensor, Γ_{11} and Γ_{22}, which represent the maximum and minimum horizontal curvature of the Bouguer gravity field. We follow Andrews-Hanna et al. (*72*) and evaluate the maximum amplitude horizontal gravity gradient, Γ_{hh}:

$$\Gamma_{hh} = \begin{cases} \Gamma_{11} & if \ \Gamma_{11} > |\Gamma_{22}| \\ \Gamma_{22} & if \ \Gamma_{11} < |\Gamma_{22}| \end{cases}. \tag{S7}$$

This maximum amplitude eigenvalue (referred to as the "Bouguer gravity gradient" or "gravity gradient" in this paper) effectively quantifies the gravity gradient orthogonal to major density structures, as long as the structure dominates the local gravity gradients. For this parameter, an annular positive mass anomaly such as a lava-filled ring fault will be expressed as an annular negative gradient anomaly centered over the feature flanked by concentric annular positive anomalies on either side (and vice-versa for a negative mass anomaly).

To assure that the structure of interest dominates the local gravity gradients, it is necessary that the gradients be evaluated from filtered Bouguer gravity fields to avoid the appearance of "striping" of gravitational anomalies along the spacecraft trajectory and other sources of noise. The Bouguer gravity was filtered with a low-pass filter applied at degree and order 600, corresponding to a block size of 9 km. To further smooth the gravity gradients, the field was calculated on a spherical reference surface at a radius of 1740 km, with the upward continuation of the gravity anomalies to this surface having a smoothing effect on shorter wavelengths. At low degree and order, topography in the mantle (such as the mantle uplift beneath Orientale) dominates the curvature in the Bouguer gravity field, and thus the gravity gradient. To highlight shorter wavelengths, and smaller density anomalies, we filtered the Bouguer gravity field with a high-pass filter, removing long-wavelength ($l \lesssim 50$) anomalies. It is important to note that Bouguer gravity gradients can produce spurious features in gravity gradient maps because of the highly non-linear action of evaluating gravity gradients and determining eigenvalues. We have avoided use of the minimum eigenvalue, which is particularly susceptible to this issue.
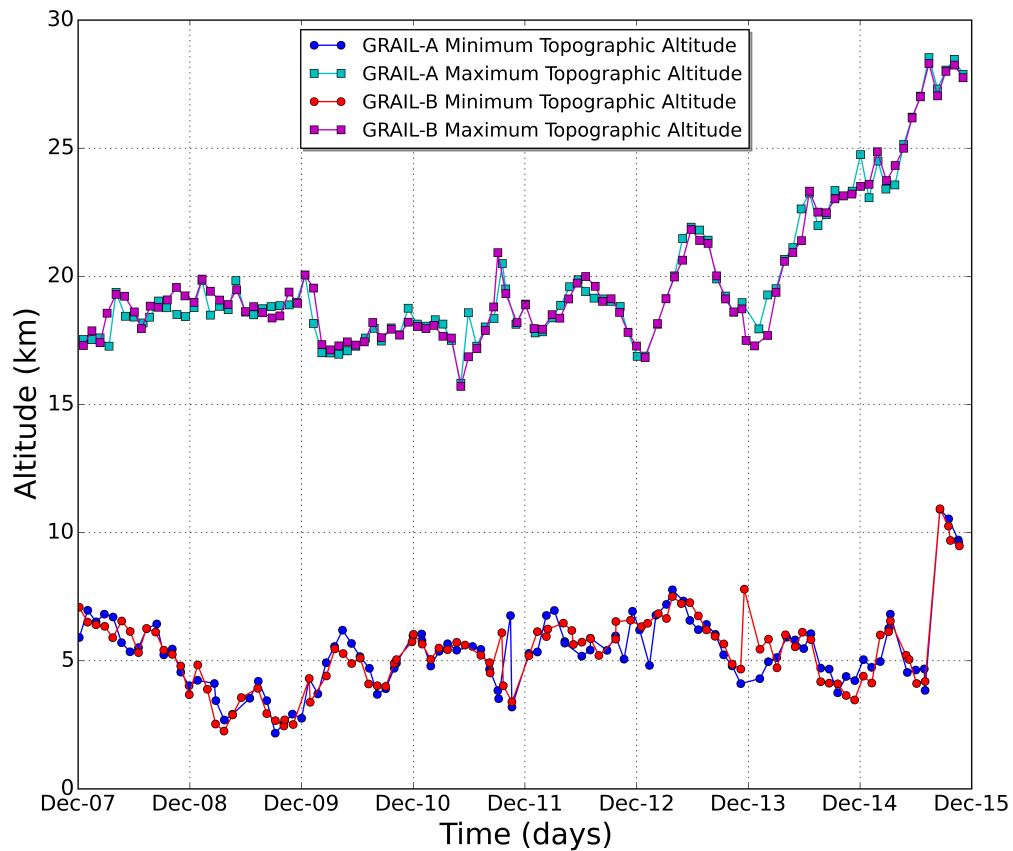
Fig.S1. GRAIL orbit evolution. Apoapsis (green, violet) and periapsis (blue, red) altitudes of GRAIL-A (Ebb) and GRAIL-B (Flow) during the GRAIL mission Endgame phase.
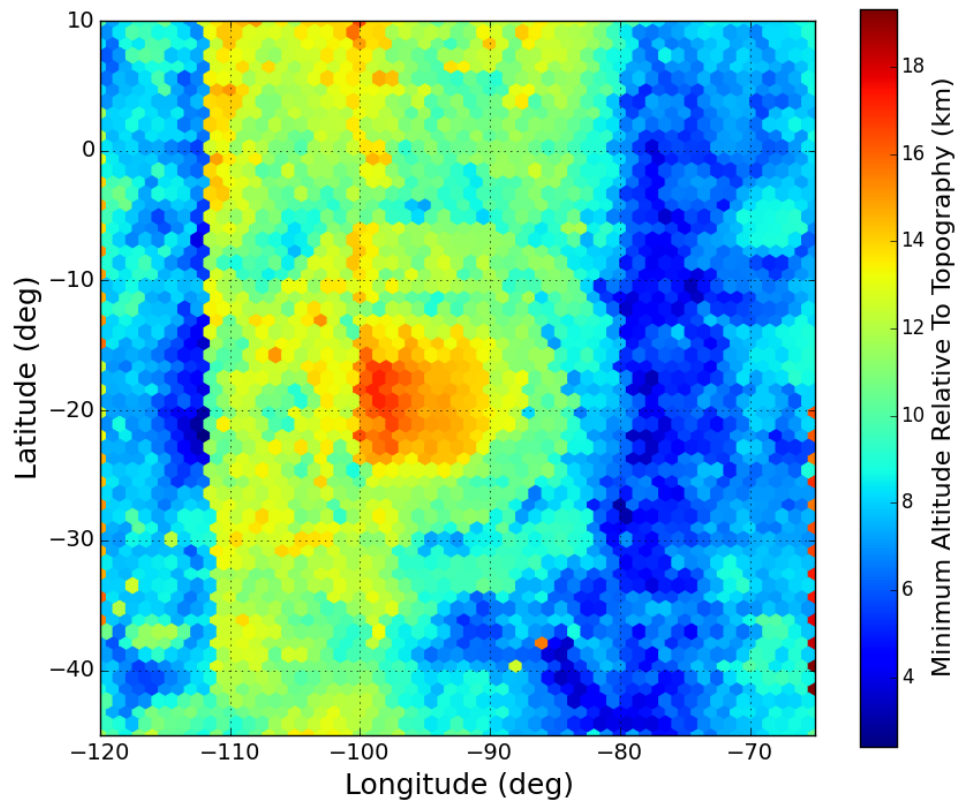
Fig. S2. Minimum mapping altitude. Minimum altitude above topography of the GRAIL dual spacecraft over the Orientale basin and surroundings.
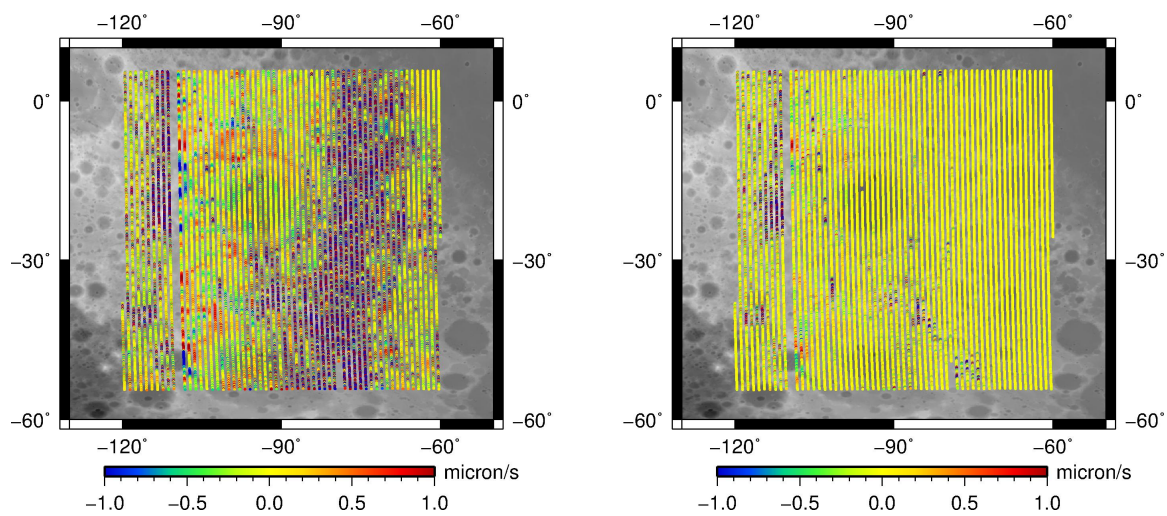
Fig. S3. Gravity residuals. **(A)** KBRR residuals with respect to a GRAIL degree-and-order-900 gravity model (*11*) over the Orientale basin and **(B)** residuals after local modeling with a smoothing factor of 10⁻³ (*49*).
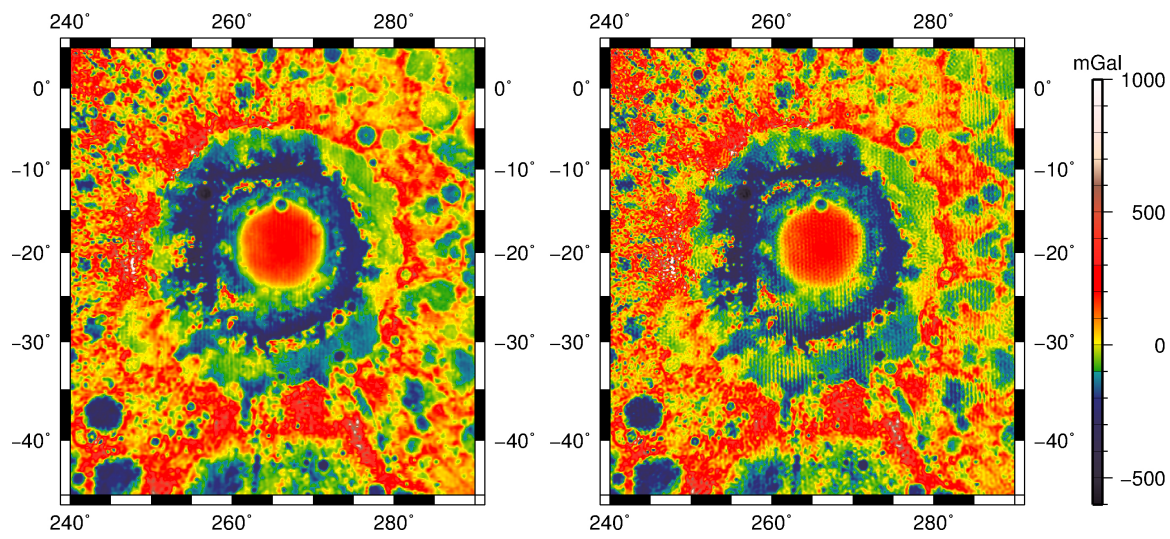
Fig. S4. Solution comparison. Free-air anomaly fields for the Orientale basin from the GRAIL mission using two independent approaches to achieve high resolution. (A) Local model with neighbor smoothing for a scaling factor of 10^{-3} as described by Goossens et al. *(49)*, and **(B)** degree-1200 spherical harmonic solution plotted to degree and order 900.
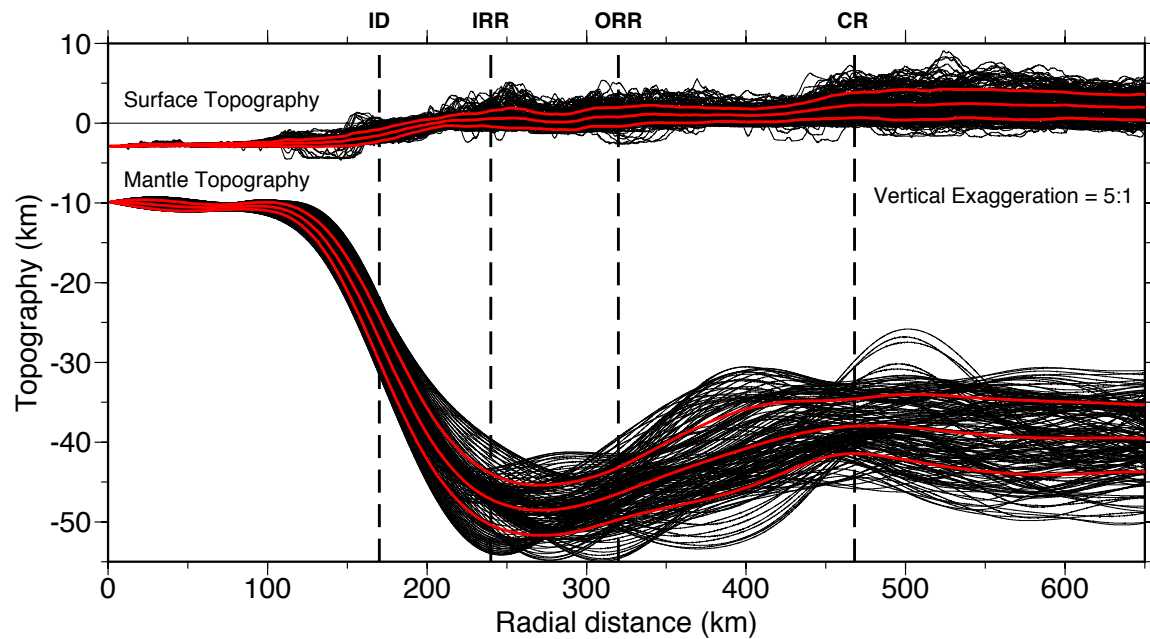
Fig. S5. Azimuthally-averaged structure. Radial profiles of surface topography and mantle relief (in black) across the Orientale basin. Basin center is at far left. Radial averages and standard deviations are plotted in red. The average positions of the basin rings are marked with vertical dashed lines (from left to right): Inner Depression, Inner Rook ring, Outer Rook ring, and Cordillera ring. Vertical exaggeration = 5:1.
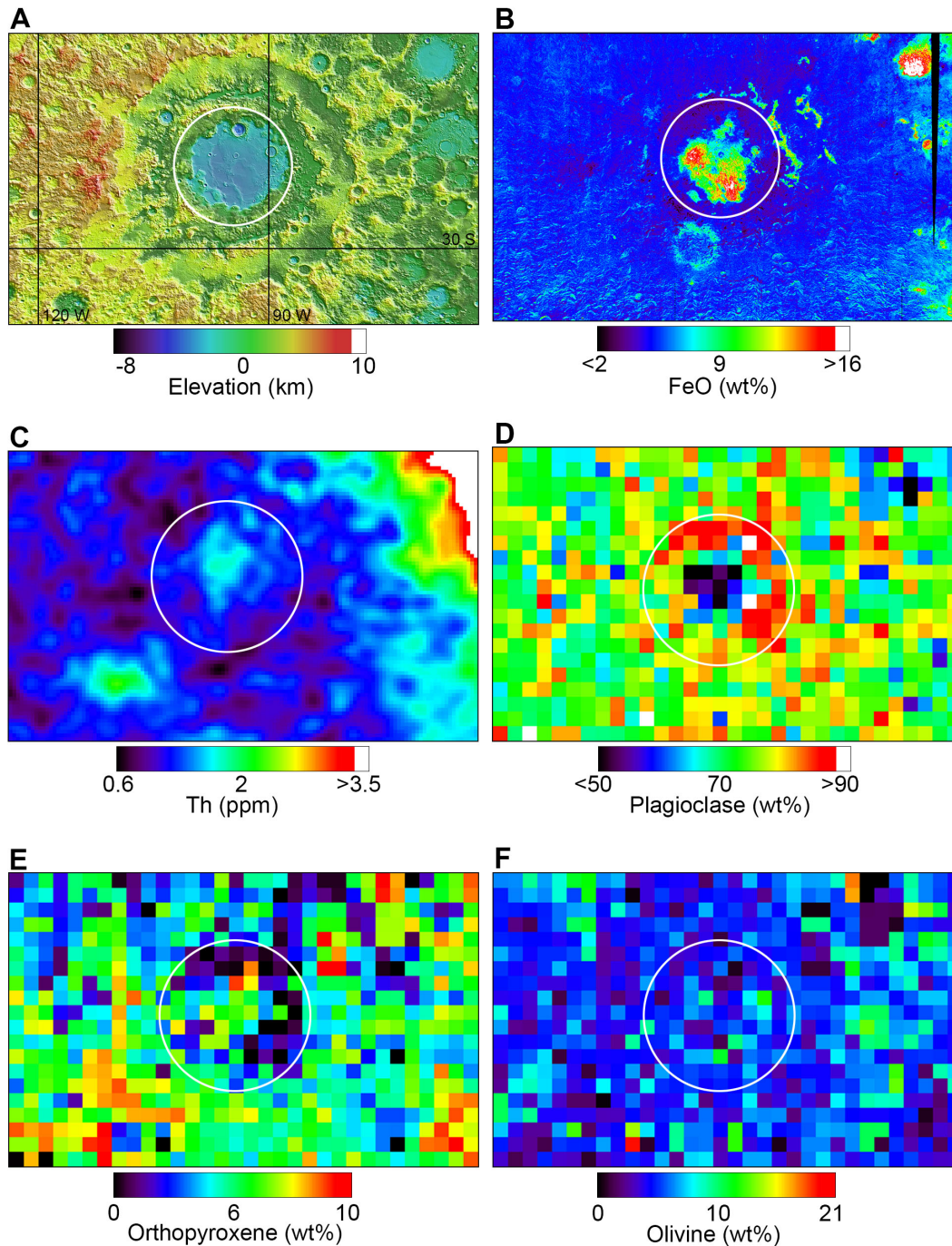
Fig. S6. Topography and compositional maps. (A) Topography, **(B)** FeO concentration, **(C)** Th concentration, **(D)** plagioclase abundance, **(E)** orthopyroxene abundance, and **(F)** olivine abundance for the Orientale basin and nearby areas. The position of the Inner Rook ring is shown in white for reference. Data sources: Topography updated from Lunar Observer Laser Altimeter (LOLA), map LDEM_64, 0.015625° spatial resolution (*74*); FeO from Clementine-derived ratio of reflectance at 950 nm wavelength to that at 750 nm, 1-km gridded data converted to FeO with the algorithm developed by Lucey et al. (*60*); Th from Lunar Prospector 0.5° data.; mineral maps from Crites and Lucey (*62*).
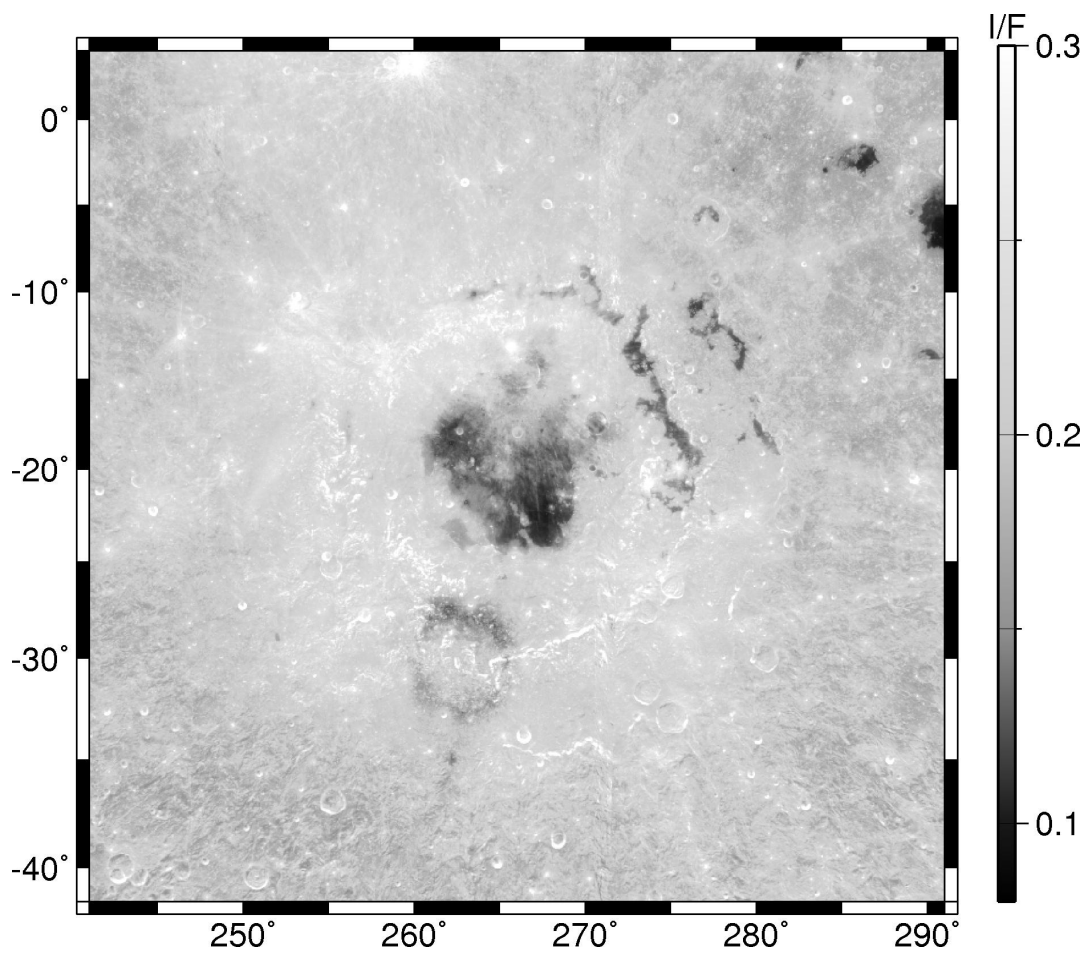
Fig. S7. Orientale crust and mare fill. Lunar Reconnaissance Orbiter Wide Angle Camera (LRO/WAC) image [WAC_GLOBAL_E000N1800_032P.img] of the Orientale basin and surroundings showing distribution of highland anorthosite crust (light) and maria (dark). The dark ring in the southern part of the basin centered on the Outer Rook ring is the product of a basaltic pyroclastic eruption from a central vent (*75*).
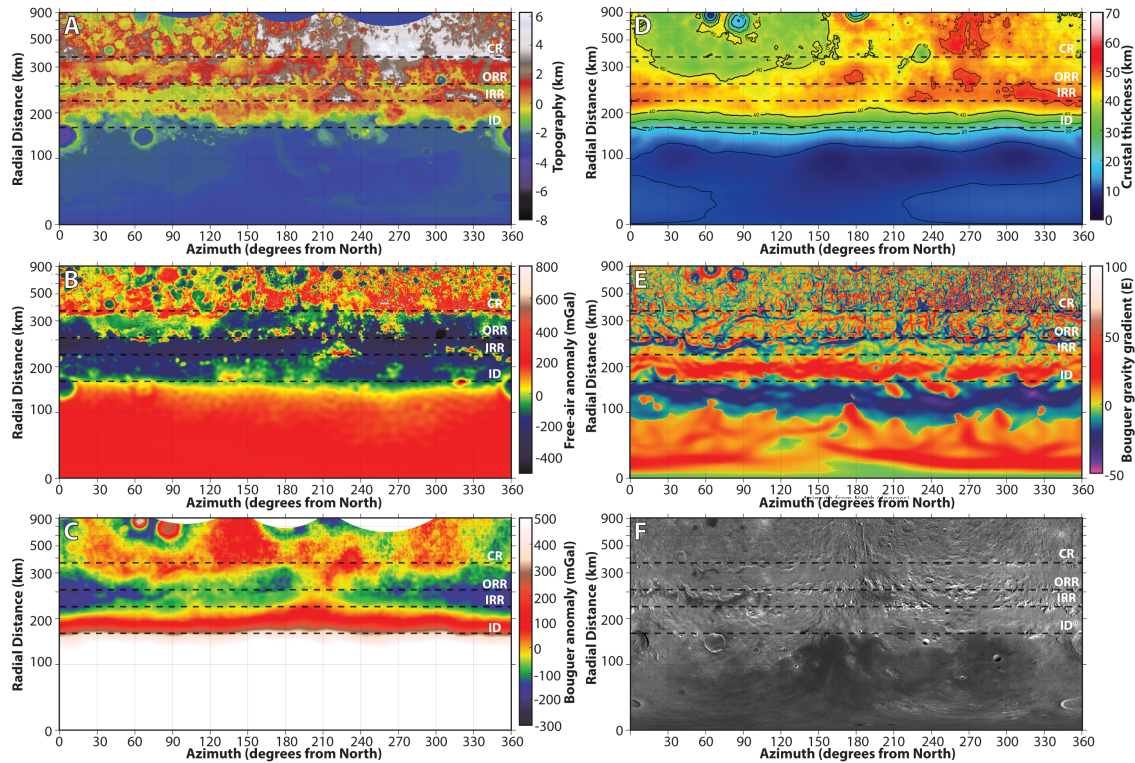
Fig. S8. "Unwrapped" polar coordinate maps. (A) Topography, **(B)** free-air gravity anomaly, **(C)** Bouguer gravity anomaly, (**D**) crustal thickness, **(E)** Bouguer gravity gradient (1 Eotovos = 10^{-4} mGal m^{-1}), and **(F)** LRO/WAC global morphology map (described in the caption to Fig. S7) with respect to the center of the Orientale basin, encompassing longitudes 240° to 295° E and latitudes -42° to 10°N. This polar projection highlights annular structures, which appear horizontal, and radial structures, which appear as vertical fabric. The center of the basin (-19.3°N, 266.0° E) is stretched along the abscissa at zero radial distance, and the radial distance of 700-km corresponds to the distal extent of the basin. The approximate locations of the Inner Depression (radial distance r=170.5 km), Inner Rook ring (r=240.5 km), Outer Rook ring (r=319.5 km), and Cordillera (r=468.5 km) are indicated by dashed lines.

References

1. D. E. Wilhelms, *The Geologic History of the Moon*. U.S. Geol. Survey Prof. Paper 1348 (U.S. Government Printing Office, Washington, DC, 1987).

2. P. D. Spudis, *The Geology of Multiring Impact Basins: The Moon and Other Planets* (Cambridge Univ. Press, Cambridge, England, 1993).

3. M. T. Zuber, D. E. Smith, D. H. Lehman, T. L. Hoffman, S. W. Asmar, M. M. Watkins, Gravity Recovery and Interior Laboratory (GRAIL): Mapping the lunar interior from crust to core. *Space Sci. Rev.* **178**, 3–24 (2013). [doi:10.1007/s11214-012-9952-7](doi:10.1007/s11214-012-9952-7)

4. D. Stöffler, G. Ryder, B. A. Ivanov, N. A. Artemieva, M. J. Cintala, R. A. F. Grieve, Cratering history and lunar chronology. *Rev. Mineral. Geochem.* **60**, 519–596 (2006). [doi:10.2138/rmg.2006.60.05](doi:10.2138/rmg.2006.60.05)

5. J. W. Head, Orientale multi-ringed basin interior and implications for the petrogenesis of lunar highland samples. *Moon* **11**, 327–356 (1974). [doi:10.1007/BF00589168](doi:10.1007/BF00589168)

6. C. I. Fassett, J. W. Head, S. J. Kadish, E. Mazarico, G. A. Neumann, D. E. Smith, M. T. Zuber, Lunar impact basins: Stratigraphy, sequence and ages from superposed impact crater populations measured from Lunar Orbiter Laser Altimeter (LOLA) data. *J. Geophys. Res.* **117**, E00H06 (2012). [doi:10.1029/2011JE003951](doi:10.1029/2011JE003951)

7. K. A. Howard, D. E. Wilhelms, D. H. Scott, Lunar basin formation and highland stratigraphy. *Rev. Geophys. Space Phys.* **12**, 309–327 (1974). [doi:10.1029/RG012i003p00309](doi:10.1029/RG012i003p00309)

8. T. H. Sweetser, M. S. Wallace, S. J. Hatch, R. B. Roncoli, Design of an Extended Mission for GRAIL, in *AIAA Astrodynamics Specialist Conference* (Minneapolis, MN, 2012) (2012), 18 pp..

9. Materials and methods are available as supplementary materials on *Science* Online.

10. D. D. Rowlands, R. D. Ray, D. S. Chinn, F. G. Lemoine, Short-arc analysis of intersatellite tracking data in a gravity mapping mission. *J. Geod.* **76**, 307–316 (2002). [doi:10.1007/s00190-002-0255-8](doi:10.1007/s00190-002-0255-8)

11. F. G. Lemoine, S. Goossens, T. J. Sabaka, J. B. Nicholas, E. Mazarico, D. D. Rowlands, B. D. Loomis, D. S. Chinn, G. A. Neumann, D. E. Smith, M. T. Zuber, GRGM900C: A degree 900 lunar gravity model from GRAIL primary and extended mission data. *Geophys. Res. Lett.* **41**, 3382–3389 (2014). Medline [doi:10.1002/2014GL060027](doi:10.1002/2014GL060027)

12. D. E. Smith, M. T. Zuber, G. A. Neumann, E. Mazarico, F. G. Lemoine, J. W. Head III, P. G. Lucey, O. Aharonson, M. S. Robinson, X. Sun, M. H. Torrence, M. K. Barker, J. Oberst, T. C. Duxbury, D. Mao, O. S. Barnouin, K. Jha, D. D. Rowlands, S. Goossens, D. Baker, S. Bauer, P. Gläser, M. Lemelin, M. Rosenburg, M. M. Sori, J. Whitten, T. Mcclanahan, Summary of the results from the Lunar Orbiter Laser Altimeter after seven years in lunar orbit. *Icarus* (2016). doi:10.1016/j.icarus.2016.06.006

13. D. E. Smith, M. T. Zuber, G. B. Jackson, J. F. Cavanaugh, G. A. Neumann, H. Riris, X. Sun, R. S. Zellar, C. Coltharp, J. Connelly, R. B. Katz, I. Kleyner, P. Liiva, A. Matuszeski, E. M. Mazarico, J. F. McGarry, A.-M. Novo-Gradac, M. N. Ott, C. Peters, L. A. Ramos-Izquierdo, L. Ramsey, D. D. Rowlands, S. Schmidt, V. S. Scott, G. B. Shaw, J. C. Smith, J.-P. Swinski, M. H. Torrence, G. Unger, A. W. Yu, T. W. Zagwodzki, The Lunar Orbiter Laser Altimeter

investigation on the Lunar Reconnaissance Orbiter mission. *Space Sci. Rev.* **150**, 209–241 (2010). doi:10.1007/s11214-009-9512-y

14. M. T. Zuber, D. E. Smith, M. M. Watkins, S. W. Asmar, A. S. Konopliv, F. G. Lemoine, H. J. Melosh, G. A. Neumann, R. J. Phillips, S. C. Solomon, M. A. Wieczorek, J. G. Williams, S. J. Goossens, G. Kruizinga, E. Mazarico, R. S. Park, D. N. Yuan, Gravity field of the Moon from the Gravity Recovery and Interior Laboratory (GRAIL) mission. *Science* **339**, 668–671 (2013). Medline doi:10.1126/science.1231507

15. Y. N. Kattoum, J. C. Andrews-Hanna, Evidence for ring-faults around the Orientale basin on the Moon from gravity. *Icarus* **226**, 694–707 (2013). doi:10.1016/j.icarus.2013.06.025

16. B. C. Johnson, D. M. Blair, G. S. Collins, H. J. Melosh, A. M. Freed, G. J. Taylor, J. W. Head, M. A. Wieczorek, J. C. Andrews-Hanna, F. Nimmo, J. T. Keane, K. Miljković, J. M. Soderblom, M. T. Zuber, The formation of the Orientale lunar multi-ring basin. *Science* **354**, 441–444 (2016).

17. J. W. Head, in *Impact and Explosion Cratering,* D. J. Roddy, R. O. Pepin, R. B. Merrill, Eds. (Pergamon Press, New York, NY, 1977), pp. 563–573.

18. C. A. Hodges, D. E. Wilhelms, Formation of lunar basin rings. *Icarus* **34**, 294–323 (1978). doi:10.1016/0019-1035(78)90169-0

19. J. W. Head, Transition from complex craters to multi-ringed basins on terrestrial planetary bodies: Scale-dependent role of the expanding melt cavity and progressive interaction with the displaced zone. *Geophys. Res. Lett.* **37**, L02203 (2010). doi:10.1029/2009GL041790

20. M. A. Wieczorek, G. A. Neumann, F. Nimmo, W. S. Kiefer, G. J. Taylor, H. J. Melosh, R. J. Phillips, S. C. Solomon, J. C. Andrews-Hanna, S. W. Asmar, A. S. Konopliv, F. G. Lemoine, D. E. Smith, M. M. Watkins, J. G. Williams, M. T. Zuber, The crust of the Moon as seen by GRAIL. *Science* **339**, 671–675 (2013). Medline doi:10.1126/science.1231530

21. M. A. Wieczorek, R. J. Phillips, Lunar multiring basins and the cratering process. *Icarus* **139**, 246–259 (1999). doi:10.1006/icar.1999.6102

22. M. A. Wieczorek, B. L. Jolliff, A. Khan, M. E. Pritchard, B. P. Weiss, J. G. Williams, L. L. Hood, K. Righter, C. R. Neal, C. K. Shearer, I. S. McCallum, S. Tompkins, B. R. Hawke, C. Peterson, J. J. Gillis, B. Bussey, The constitution and structure of the lunar interior. *Rev. Mineral. Geochem.* **60**, 221–364 (2006). doi:10.2138/rmg.2006.60.3

23. M. Xie, M.-H. Zhu, Estimates of primary ejecta and local material for the Orientale basin: Implications for the formation and ballistic sedimentation of multi-ring basins. *Earth Planet. Sci. Lett.* **440**, 71–80 (2016). doi:10.1016/j.epsl.2016.02.012

24. J. Besserer, F. Nimmo, M. A. Wieczorek, R. C. Weber, W. S. Kiefer, P. J. McGovern, J. C. Andrews-Hanna, D. E. Smith, M. T. Zuber, GRAIL gravity constraints on the vertical and lateral density structure of the lunar crust. *Geophys. Res. Lett.* **41**, 5771–5777 (2014). doi:10.1002/2014GL060240

25. W. S. Kiefer, R. J. Macke, D. T. Britt, A. J. Irving, G. J. Consolmagno, The density and porosity of lunar rocks. *Geophys. Res. Lett.* **39**, L07201 (2012). doi:10.1029/2012GL051319

26. M. T. Zuber, D. E. Smith, F. G. Lemoine, G. A. Neumann, The shape and internal structure of the moon from the clementine mission. *Science* **266**, 1839–1843 (1994). Medline doi:10.1126/science.266.5192.1839

27. G. A. Neumann, M. T. Zuber, D. E. Smith, F. G. Lemoine, The lunar crust: Global structure and signature of major basins. *J. Geophys. Res.* **101**, 16841–16863 (1996). doi:10.1029/96JE01246

28. A. S. Konopliv, A. B. Binder, L. L. Hood, A. B. Kucinskas, W. L. Sjogren, J. G. Williams, Improved gravity field of the moon from lunar prospector. *Science* **281**, 1476–1480 (1998). Medline doi:10.1126/science.281.5382.1476

29. N. Namiki, T. Iwata, K. Matsumoto, H. Hanada, H. Noda, S. Goossens, M. Ogawa, N. Kawano, K. Asari, S. I. Tsuruta, Y. Ishihara, Q. Liu, F. Kikuchi, T. Ishikawa, S. Sasaki, C. Aoshima, K. Kurosawa, S. Sugita, T. Takano, Farside gravity field of the moon from four-way Doppler measurements of SELENE (Kaguya). *Science* **323**, 900–905 (2009). Medline doi:10.1126/science.1168029

30. P. M. Muller, W. L. Sjogren, Mascons: Lunar mass concentrations. *Science* **161**, 680–684 (1968). Medline doi:10.1126/science.161.3842.680

31. J. C. Andrews-Hanna, The origin of the non-mare mascon gravity anomalies in lunar basins. *Icarus* **222**, 159–168 (2013). doi:10.1016/j.icarus.2012.10.031

32. H. J. Melosh, A. M. Freed, B. C. Johnson, D. M. Blair, J. C. Andrews-Hanna, G. A. Neumann, R. J. Phillips, D. E. Smith, S. C. Solomon, M. A. Wieczorek, M. T. Zuber, The origin of lunar mascon basins. *Science* **340**, 1552–1555 (2013). Medline doi:10.1126/science.1235768

33. R. M. Schmidt, K. R. Housen, Some recent advances in the scaling of impact and explosion cratering. *Int. J. Impact Eng.* **5**, 543–560 (1987). doi:10.1016/0734-743X(87)90069-8

34. B. A. Ivanov, H. J. Melosh, E. Pierazzo, in *Large Meteorite Impacts and Planetary Evolution,* R. L. Gibson, W. U. Reimold, Eds. (Geological Society of America, Boulder, CO, 2010), pp. 29–49.

35. R. W. K. Potter, D. A. Kring, G. S. Collins, W. S. Kiefer, P. J. McGovern, Numerical modeling of the formation and structure of the Orientale impact basin. *J. Geophys. Res.* **118**, 1–17 (2013).

36. R. W. K. Potter, D. Kring, G. S. Collins, W. S. Kiefer, P. J. McGovern, Estimating transient crater size using the crustal annular bulge: Insights from numerical modeling of lunar basin-scale impacts. *Geophys. Res. Lett.* **39**, L18203 (2012). doi:10.1029/2012GL052981

37. G. A. Neumann, M. T. Zuber, M. A. Wieczorek, J. W. Head, D. M. Baker, S. C. Solomon, D. E. Smith, F. G. Lemoine, E. Mazarico, T. J. Sabaka, S. J. Goossens, H. J. Melosh, R. J. Phillips, S. W. Asmar, A. S. Konopliv, J. G. Williams, M. M. Sori, J. M. Soderblom, K. Miljković, J. C. Andrews-Hanna, F. Nimmo, W. S. Kiefer, Lunar impact basins revealed by Gravity Recovery and Interior Laboratory measurements. *Sci. Adv.* **1**, e1500852 (2015). Medline doi:10.1126/sciadv.1500852

38. A. Nahm, T. Öhman, D. Kring, Normal faulting origin for the Cordillera and Outer Rook Rings of Orientale Basin, the Moon. *J. Geophys. Res.* **118**, 190–205 (2013). doi:10.1002/jgre.20045

39. J. F. McCauley, Orientale and Caloris. *Phys. Earth Planet. Inter.* **15**, 220–250 (1977). doi:10.1016/0031-9201(77)90033-4

40. S. P. S. Gulick, G. L. Christeson, P. J. Barton, R. A. F. Grieve, J. V. Morgan, J. Urrutia-Fucugauchi, Geophysical characterization of the Chicxulub impact crater. *Rev. Geophys. Space Phys.* **51**, 31–52 (2013). [doi:10.1002/rog.20007](doi:10.1002/rog.20007)

41. S. J. Hatch, R. B. Roncoli, T. H. Sweetser, GRAIL trajectory design: Lunar orbit insertion through science in *AIAA Astrodynamics Conference* (Toronto, 2010), vol. AIAA 2010-8385 (2010).

42. G. Beerer, G. G. Havens, Operating the Dual-Orbiter GRAIL Mission to Measure the Moon's Gravity, paper presented at SpaceOps 2012, 11–15 June 2012.

43. A. S. Konopliv, R. S. Park, D.-N. Yuan, S. W. Asmar, M. M. Watkins, J. G. Williams, E. Fahnestock, G. Kruizinga, M. Paik, D. Strekalov, N. Harvey, D. E. Smith, M. T. Zuber, The JPL lunar gravity field to spherical harmonic degree 660 from the GRAIL Primary Mission. *J. Geophys. Res.* **118**, 1415–1434 (2013). doi:10.1002/jgre.20097

44. F. G. Lemoine, S. Goossens, T. J. Sabaka, J. B. Nicholas, E. Mazarico, D. D. Rowlands, B. D. Loomis, D. S. Chinn, D. S. Caprette, G. A. Neumann, D. E. Smith, M. T. Zuber, High-degree gravity models from GRAIL primary mission data. *J. Geophys. Res.* **118**, 1676–1698 (2013). doi:10.1002/jgre.20118

45. A. S. Konopliv, R. S. Park, D.-N. Yuan, S. W. Asmar, M. M. Watkins, J. G. Williams, E. Fahnestock, G. Kruizinga, M. Paik, D. Strekalov, N. Harvey, D. E. Smith, M. T. Zuber, JPL high resolution lunar gravity fields from the GRAIL Primary and Extended mission. *Geophys. Res. Lett.* **41**, 1452–1458 (2014). [doi:10.1002/2013GL059066](doi:10.1002/2013GL059066)

46. D. D. Rowlands, S. B. Luthcke, S. M. Klosko, F. G. R. Lemoine, D. S. Chinn, J. J. McCarthy, C. M. Cox, O. B. Anderson, Resolving mass flux at high spatial and temporal resolution using GRACE intersatellite measurements. *Geophys. Res. Lett.* **32**, L04310 (2005). [doi:10.1029/2004GL021908](doi:10.1029/2004GL021908)

47. S. B. Luthcke, D. D. Rowlands, F. G. Lemoine, S. M. Klosko, D. Chinn, J. J. McCarthy, Monthly spherical harmonic gravity field solutions determined from GRACE inter-satellite range-rate data alone. *Geophys. Res. Lett.* **33**, L02402 (2006). [doi:10.1029/2005GL024846](doi:10.1029/2005GL024846)

48. B. D. Tapley, S. Bettadpur, J. C. Ries, P. F. Thompson, M. M. Watkins, GRACE measurements of mass variability in the Earth system. *Science* **305**, 503–505 (2004). Medline doi:10.1126/science.1099192

49. S. Goossens, T. J. Sabaka, J. B. Nicholas, F. G. Lemoine, D. D. Rowlands, E. Mazarico, G. A. Neumann, D. E. Smith, M. T. Zuber, High-resolution local gravity model of the south pole of the Moon from GRAIL extended mission data. *Geophys. Res. Lett.* **41**, 3367–3374 (2014). Medline [doi:10.1002/2014GL060178](doi:10.1002/2014GL060178)

50. W. A. Heiskanen, H. Moritz, *Physical Geodesy* (W. H. Freeman, San Francisco/London, 1967).

51. D. E. Pavlis, J. Wimert, J. J. McCarthy, *GEODYN II System Description*, vol. 1-5 (Stinger Ghaffarian Technologies, 2013).

52. D. D. Rowlands, S. B. Luthcke, J. J. McCarthy, S. M. Klosko, D. S. Chinn, F. G. Lemoine, J.-P. Boy, T. J. Sabaka, Global mass flux solutions from GRACE: A comparison of parameter estimation strategies–Mass concentrations versus Stokes coefficients. *J. Geophys. Res.* **115**, B01403 (2010). [doi:10.1029/2009JB006546](doi:10.1029/2009JB006546)

53. T. J. Sabaka, D. D. Rowlands, S. B. Luthcke, J.-B. Boy, Improving global mass flux solutions from Gravity Recovery and Climate Experiment (GRACE) through forward modeling and continuous time correlation. *J. Geophys. Res.* **115**, B11403 (2010). doi:10.1029/2010JB007533

54. A. M. Freed, B. C. Johnson, D. M. Blair, H. J. Melosh, G. A. Neumann, R. J. Phillips, S. C. Solomon, M. A. Wieczorek, M. T. Zuber, The formation of lunar mascon basins from impact to contemporary form. *J. Geophys. Res.* **119**, 2378–2397 (2014). doi:10.1002/2014JE004657

55. P. D. Spudis, D. J. P. Martin, G. Y. Kramer, Geology and composition of the Orientale Basin impact melt sheet. *J. Geophys. Res.* **119**, 1–11 (2014).

56. Q. Huang, M. A. Wieczorek, Density and porosity of the lunar crust from gravity and topography. *J. Geophys. Res.* **117**, (2012). doi:10.1029/2012JE004062

57. B. L. Jolliff, J. J. Gillis, L. Haskin, R. L. Korotev, M. A. Wieczorek, Major lunar crustal terranes: Surface expressions and crust-mantle origins. *J. Geophys. Res.* **105**, 4197–4216 (2000). doi:10.1029/1999JE001103

58. R. L. Korotev, The great lunar hot spot and the composition and origin of the Apollo mafic ("LKFM") impact-melt breccias. *J. Geophys. Res.* **105**, 4317–4345 (2000). doi:10.1029/1999JE001063

59. J. J. Papike, G. Ryder, C. K. Shearer, in *Planetary Materials,* J. J. Papike, Ed., vol. 36, Rev. Mineral., 36, pp. 5-1 to 5-235 (1998).

60. P. G. Lucey, D. T. Blewett, B. J. Jolliff, Lunar iron and titanium abundance algorithms based on final processing of Clementine ultraviolet-visible images. *J. Geophys. Res.* **105**, 20297–20305 (2000). doi:10.1029/1999JE001117

61. T. H. Prettyman, J. J. Hagerty, R. C. Elphic, W. C. Feldman, D. J. Lawrence, G. W. McKinney, D. T. Vaniman, Elemental composition of the lunar surface: Analysis of gamma ray spectroscopy data from Lunar Prospector. *J. Geophys. Res.* **111**, E12007 (2006). doi:10.1029/2005JE002656

62. S. T. Crites, P. D. Lucey, Revised mineral and Mg# maps of the Moon from integrating results from the Lunar Prospector neutron and gamma-ray spectrometers with Clementine spectroscopy. *Am. Mineral.* **100**, 973–982 (2015). doi:10.2138/am-2015-4874

63. P. D. Lucey, Mineral maps of the Moon. *Geophys. Res. Lett.* **31**, L08701 (2004). doi:10.1029/2003GL019406

64. W. M. Vaughan, J. W. Head, L. Wilson, P. C. Hess, Geology and petrology of enormous volumes of impact melt on the Moon: A case study of the Orientale basin impact melt sea. *Icarus* **223**, 749–765 (2013). doi:10.1016/j.icarus.2013.01.017

65. H. J. Moore, C. A. Hodges, D. H. Scott, Multi-ringed basins–Illustrated by Orientale and associated features. *Proc. Lunar Planet. Sci. Conf. 5th, Geochim. Cosmochim. Acta supp. 5*, 71–100 (1974).

66. S. Yamamoto, R. Nakamura, T. Matsunaga, Y. Ogawa, Y. Ishihara, T. Morota, N. Hirata, M. Ohtake, T. Hiroi, Y. Yokota, J. Haruyama, Massive layer of pure anorthosite on the Moon. *Geophys. Res. Lett.* **39**, L13201 (2012). doi:10.1029/2012GL052098

67. L. C. Cheek, K. L. Donaldson Hanna, C. M. Pieters, J. W. Head, J. L. Whitten, Distribution and purity of anorthosite across the Orientale basin: New perspectives from Moon Mineralogy Mapper data. *J. Geophys. Res.* **118**, 1–16 (2013).

68. P. Lognonné, J. Gagnepain-Beyneix, H. Chenet, A new seismic model for the Moon: Implications for structure, thermal evolution and formation of the Moon. *Earth Planet. Sci. Lett.* **211**, 27–44 (2003). doi:10.1016/S0012-821X(03)00172-9

69. A. Khan, K. Mosegaard, An inquiry into the lunar interior: A nonlinear inversion of the Apollo lunar seismic data. *J. Geophys. Res.* **107**, 5036 (2002). doi:10.1029/2001JE001658

70. C. I. Fassett, J. W. I. Head, D. E. Smith, M. T. Zuber, G. A. Neumann, Thickness of proximal ejecta from the Orientale Basin from Lunar Orbiter Laser Altimeter (LOLA) data: Implications for multi-ring basin formation. *Geophys. Res. Lett.* **38**, L17201 (2011). doi:10.1029/2011GL048502

71. V. L. Sharpton, Outcrops on lunar crater rims: Implications for rim construction, mechanisms, ejecta volumes and excavation depths. *J. Geophys. Res. Planets* **119**, 154–168 (2014). doi:10.1002/2013JE004523

72. J. C. Andrews-Hanna, S. W. Asmar, J. W. Head, W. S. Kiefer, A. S. Konopliv, F. G. Lemoine, I. Matsuyama, E. Mazarico, P. J. McGovern, H. J. Melosh, G. A. Neumann, F. Nimmo, R. J. Phillips, D. E. Smith, S. C. Solomon, G. J. Taylor, M. A. Wieczorek, J. G. Williams, M. T. Zuber, Ancient igneous intrusions and early expansion of the moon revealed by GRAIL gravity gradiometry. *Science* **339**, 675–678 (2013). doi:10.1126/science.1231753

73. J. C. Andrews-Hanna, J. Besserer, J. W. Head 3rd, C. J. Howett, W. S. Kiefer, P. J. Lucey, P. J. McGovern, H. J. Melosh, G. A. Neumann, R. J. Phillips, P. M. Schenk, D. E. Smith, S. C. Solomon, M. T. Zuber, Structure and evolution of the lunar Procellarum region as revealed by GRAIL gravity data. *Nature* **514**, 68–71 (2014). Medline doi:10.1038/nature13697

74. D. E. Smith, M. T. Zuber, G. A. Neumann, F. G. Lemoine, E. Mazarico, M. H. Torrence, J. F. McGarry, D. D. Rowlands, J. W. Head III, T. H. Duxbury, O. Aharonson, P. G. Lucey, M. S. Robinson, O. S. Barnouin, J. F. Cavanaugh, X. Sun, P. Liiva, D.- Mao, J. C. Smith, A. E. Bartels, Initial observations from the Lunar Orbiter Laser Altimeter (LOLA). *Geophys. Res. Lett.* **37**, L18204 (2010). doi:10.1029/2010GL043751

75. J. W. Head, C. M. Weitz, L. Wilson, Dark ring in Southwestern Orientale Basin: Origin as a single pyroclastic eruption. *J. Geophys. Res.* **107**, 5001 (2002). doi:10.1029/2000JE001438